ARMY RESEARCH LABORATORY

2010 Neuroscience Director's Strategic Initiative

by Scott Kerick, Anthony J. Ries, Kelvin Oie, Tzyy-Ping Jung, Jeng-ren Duann, Jin-Chern Chiou, Liyi Dai, and Kaleb McDowell

ARL-TR-5457   **February 2011**

NOTICES

Disclaimers

The findings in this report are not to be construed as an official Department of the Army position unless so designated by other authorized documents.

Citation of manufacturer's or trade names does not constitute an official endorsement or approval of the use thereof.

Destroy this report when it is no longer needed. Do not return it to the originator.

Army Research Laboratory
Aberdeen Proving Ground, MD 21005

2010 Neuroscience Director's Strategic Initiative

Scott Kerick, Anthony J. Ries, Kelvin Oie, and Kaleb McDowell
Human Research and Engineering Directorate, ARL

Tzyy-Ping Jung, Jeng-ren Duann, and Jin-Chern Chiou
Swartz Center for Computational Neuroscience,
University of California, San Diego

Liyi Dai
U.S. Army Research Office

REPORT DOCUMENTATION PAGE		*Form Approved* *OMB No. 0704-0188*

1. REPORT DATE *(DD-MM-YYYY)*	2. REPORT TYPE	3. DATES COVERED (From - To)
February 2011	DSI	

4. TITLE AND SUBTITLE	5a. CONTRACT NUMBER
2010 Neuroscience Director's Strategic Initiative	
	5b. GRANT NUMBER
	5c. PROGRAM ELEMENT NUMBER

6. AUTHOR(S)	5d. PROJECT NUMBER
Scott Kerick, Anthony J. Ries, Kelvin Oie, Tzyy-Ping Jung, Jeng-ren Duann, Jin-Chern Chiou, Liyi Dai, and Kaleb McDowell	
	5e. TASK NUMBER
	5f. WORK UNIT NUMBER

7. PERFORMING ORGANIZATION NAME(S) AND ADDRESS(ES)	8. PERFORMING ORGANIZATION REPORT NUMBER
U.S. Army Research Laboratory ATTN: RDRL-HRS-B Aberdeen Proving Ground, MD 21005	ARL-TR-5457

9. SPONSORING/MONITORING AGENCY NAME(S) AND ADDRESS(ES)	10. SPONSOR/MONITOR'S ACRONYM(S)
	11. SPONSOR/MONITOR'S REPORT NUMBER(S)

12. DISTRIBUTION/AVAILABILITY STATEMENT

Approved for public release; distribution unlimited.

13. SUPPLEMENTARY NOTES

14. ABSTRACT

Understanding how Soldiers' cognitive abilities meet the increasing demands of dynamic, complex, and stressful environments is critical for the development of systems that optimize mission effectiveness and maximize Soldier survivability. In order to acquire, monitor, and assess Soldier sensory, perceptual, emotional, cognitive, and physical performance within realistic operational environments, new technologies must be further developed to enable sensing capabilities in these dynamic environments, and innovative research paradigms and data analysis methods must be enhanced, validated, and transitioned into system designs. Thus, the 2010 Neuroscience Director's Strategic Initiative (DSI) research aims to advance neuroscientific methodologies and technologies to enable revolutionary advances in Soldier-system performance by integrating modern neuroscience with human factors, psychology, and engineering. This report covers three independent projects supporting this effort. First, Tzyy-Ping Jung and colleagues (University of California, San Diego) present their advances in developing a neuroimaging system comprised of electro-optode sensors for simultaneous recording of electroencephalography (EEG) and functional near-infrared spectroscopy (fNIRS) from Soldiers in operational environments. Second, Anthony Ries and Kaleb McDowell (U.S. Army Research Laboratory [ARL]) outline their testing and evaluation of a brain state classification algorithm from EEG data acquired from participants performing tasks with varied cognitive demands. Third, Kaleb McDowell, Scott Kerick, and Kelvin Oie (ARL) report on their implementation of a new nonlinear signal processing algorithm on EEG data acquired from participants performing a task in noisy environments.

15. SUBJECT TERMS

electroencephalography, EEG, phase lag index, functional near-infrared, fNIR, pattern classification

16. SECURITY CLASSIFICATION OF:			17. LIMITATION OF ABSTRACT	18. NUMBER OF PAGES	19a. NAME OF RESPONSIBLE PERSON Scott Kerick
a. REPORT	b. ABSTRACT	c. THIS PAGE	UU	42	19b. TELEPHONE NUMBER *(Include area code)* (410) 278-5833
Unclassified	Unclassified	Unclassified			

Standard Form 298 (Rev. 8/98)
Prescribed by ANSI Std. Z39.18

Contents

List of Figures

List of Tables

1. Project 1: Simultaneous EEG and NIRS Tomographic Imaging Based on New Electro-Optodes

1.1 Authors

The authors on this project are Tzyy-Ping Jung, Jeng-ren Duann, and Jin-Chern Chiou from the Institute for Neural Computation, University of California, San Diego, La Jolla, CA.

1.2 Introduction/Objective

This study aims to design, fabricate, and test a truly portable, lightweight, noninvasive, neuroimaging system that supports simultaneous electroencephalographic (EEG) and functional near-infrared spectroscopic (fNIRS) acquisition to provide complementary information of the brain. The acquired neural dynamics could be comparable to those obtained from simultaneous EEG and functional magnetic resonance imaging (fMRI) recordings. The envisioned dual-modality neuroimaging system will feature our newly developed EEG/NIRS electrodes, known as electro-optodes, based on micro-electromechanical system (MEMS) technology and miniaturized supporting hardware and software for biological or cognitive monitoring of participants in operational environments. Another major goal of this project is to develop advanced signal-processing methods and software for (1) increasing signal-to-noise ratio of the acquired EEG and optical imaging; and (2) two-dimensional (2-D) and three-dimensional (3-D) image reconstruction and rendering to reconstruct the optical images for investigating neurovascular coupling with minimum inter-modality interferences and preparation demands.

The advantages of simultaneous EEG/fMRI recordings have been explored by many studies and received increasing attention in neuroscience community (Ives et al., 1993; Huang-Hellinger et al., 1995; Lemieux et al., 1997). However, simultaneous EEG/fMRI recordings have formidable technical problems. For example, in EEG/fMRI recording, any ferromagnetism in the scanner can be dangerous for the subject and will certainly cause unacceptable loss in the blood-oxygen-level dependence (BOLD) image. Then, small movements of the electrodes or cables in a strong magnetic field will introduce artifactual currents. The recorded EEG signals will be completely useless before the magnetic resonance (MR) artifacts can be removed. To remove the MR-induced artifacts, the onset timings and the waveforms of the MR artifacts need to be precisely registered during the acquisition of each MR image slice. This, in turn, requires high sampling rate for EEG recordings (at least 5 KHz compared with 250 Hz for regular EEG recordings). On the other hand, EEG electrodes may also introduce deformation of the magnetic field of the MR scanner and, in turn, cause signal void in (f)MR images around the scalp electrodes. All these interferences make simultaneous EEG/fMRI and post-processing extremely difficult. Therefore, a truly small, lightweight, battery-powered EEG/fMRI system for concurrent EEG/fMRI

recordings of the freely moving subjects in real-world environments will be extremely difficult, if ever possible, in the near future.

This study is integrating a novel EEG/fNIRS electro-optode that can be used as an EEG electrode and a near-infrared (NIR) light emitter and photodetector, supporting wearable data acquisition (DAQ), signal-processing, and image rendering software into a wearable neuroimaging system. We will also develop advanced 2-D and 3-D image reconstruction algorithms to reconstruct the optical images from the recorded fNIRS signals. The envisioned simultaneous EEG/fNIRS acquisition system is completely novel and different from any other currently available systems. First, the envisioned system features brand-new dry EEG/NIRS electro-optodes, which can function as an NIR emitter, a detector, and an EEG electrode without requiring any skin preparation and conductive paste. Most importantly, the electro-optode also comprises built-in NIR light sources and NIR waveguide to bypass the high reflectance of the human dead-skin layer such that low-power NIR light sources will be sufficient for high-quality recording. In addition to the innovative hardware design, fabrication, and integration, Independent Components Analysis (ICA)-based signal processing can separate the mixture signals caused by multiple light sources and multiple possible pathways. As a result, we are able to reconstruct a 3-D optical tomography, which may be more specific to the underlying BOLD effects. In turn, we should be able to better assess the interrelationship between the BOLD effects and the neural activities measured by the simultaneously recorded EEG signals.

1.3   Original Approach

This research proposed to design, fabricate, and test a truly portable, lightweight, noninvasive, neuroimaging system that supports simultaneous EEG and fNIRS acquisition to provide complementary information of the brain. The development effort was proposed according to the following schedule:

- **Year 1**: We will first develop EEG/fNIRS electro-optodes and test the safety of the newly developed electro-optode. The specific goals are to (1) observe the depth of penetration of the micro-spikes to see if they are staying in the epidermis layer without further puncturing into the papillary dermis and (2) examine the tissue damage by comparing the skin slice cut from the site with and without the applications of electro-optodes.

- **Year 2**: We will conduct the same penetration rate study listed previously on human subject's fingers but use the proposed electro-optodes with built-in light-emitting diode (LED) light source. The results of this study will be compared to those obtained from the experimenting using external NIR light sources. This comparison will help us to determine the minimum power level needed in the final implementation of the built-in LED light sources of the electro-optodes.

- **Year 3**: We propose to (1) build a 2-D sensor array with 16 (4x4) electro-optodes by first trying to arrange the 16 electro-optodes in a 4 by 4 grid with emitters and detectors placed in an interleaved fashion; and (2) establish imaging protocol(s). Since all the electro-optodes can be used as an emitter and photodetector, the montage of such 16-channel fNIRS imaging systems can be extremely flexible.

- **Year 4**: (1) We will apply the 16-channel, 2-D EEG/fNIRS acquisition patch to acquire both electromyogram (EMG) signals and optical images from the human forearms. The 4x4, 16-channel, 2-D imaging system will be applied to the inner side of the human subjects' forearms to acquire both EMG and optical images when the subjects are performing finger tapping and making-a-fist tasks. As expected, finger tapping or making a fist will involve different muscle bundles of the forearm. The muscle activities will create electric signals, hence EMG, as well as oxy- and deoxyhemoglobin concentration changes due to oxygenation of the muscle cells. The signals accrued by the envisioned system can be used to investigate the relationship between the underlying muscle oxygenations and the corresponding electric signals from the combined imaging modalities. (2) We will apply the 16-channel, 2-D simultaneous EEG/fNIRS imaging system to the human scalp with a coverage of left/right sensorimotor cortex (i.e., pre- and postcentral gyri). We will simultaneously acquire EEG and fNIRS images on the scalp from the human subjects performing the same finger tapping and making-a-fist tasks as in Year 3. In the recorded EEG signals, we expect to find the motor-related mu-rhythm activities as can be found by International 10–20 EEG systems. In addition, we will also apply the 2-D image reconstruction algorithm to the recorded fNIRS signals using the same protocol as described previously to reconstruct the fNIRS signals acquired from the human scalp.

- **Year 5**: We plan to expand the coverage of the simultaneous EEG/fNIRS image acquisition to the whole head by adopting the standard 10–20 EEG system montage. This work allows us to (1) expend the number of electro-optodes from 16 to 32 channels, (2) co-register fNIRS and EEG measurements to the MR structure scans of the individual subjects or to the standard MNI brain template, and (3) reconstruct 3-D optical images for the whole brain in cognitive studies.

1.4   Results to Date

1.4.1 Design and Development of Electro-Optodes (EEG/fNIR Sensors)

Background. Photoplethysmography (PPG) is a simple and low-cost optical technique that can be used to detect blood volume changes in a micro-vascular bed of tissue. PPG has been applied in many different clinical settings, including clinical physiological monitoring, vascular assessment, and autonomic function. Since PPG is a non-invasive method, it should not cause any damage to subjects. This study uses red and NIR light to assess brain dynamics because it is very cost effective and easy to apply and use. Further, the light source (LEDs) and detector (photodiodes [PDs]) could be easily embedded on a portable probe.

Major Progress. In the past few months, we have explored many different electronic and form factor designs for the electro-optodes, which can simultaneously measure EEG and fNIR signals. After numerous simulations and tests, we have finalized the form factor of electro-optodes and fabricated some samples for testing. This study has also developed an innovative mechanism to place the sensor to the scalp to minimize the interference from the hair to the recording.

Design. Figure 1 shows a schematic diagram of the O-shaped PPG sensor. In order to detect PPG signal, there can be one or several LEDs and photodiodes on this O-type probe.
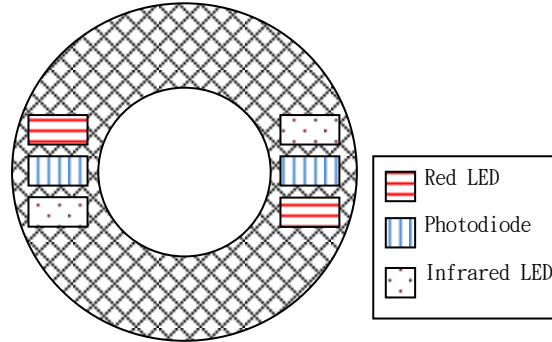
Figure 1. An O-shaped NIR sensor integrating LEDs and PDs.

Figure 2 illustrates the application of the PPG sensor to the scalp. By snipping a small strand of hair and putting them through the hole of the O-shaped sensor, the hair will be fixed and a "ring" of the skin will be exposed. The light source then can directly illuminate and reflect from the subject's scalp (as shown in figure 2).
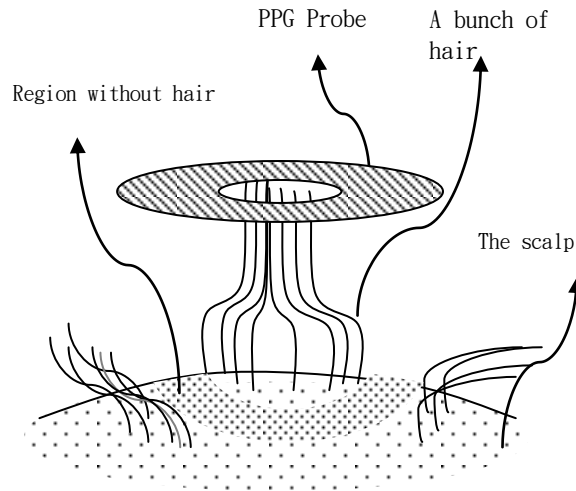
Figure 2. The application of the PPG sensor to the scalp.

Development and Implementation. Figure 3 shows the printed circuit board (PCB) and the LED/PD of the electro-optodes. The inner and outer diameters of the electro-optode are 1 cm and 2 cm, respectively. The EEG sensor is soldered to the small rectangular area shown in figure 3.
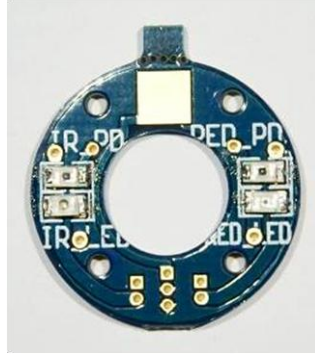
Figure 3. The final form factor
of the electro-optodes.

1.4.2 A 16-channel Analog Front-End (AFE) Amplifier

To acquire EEG and fNIR data measured by the electro-optodes, we have recently developed a 16-channel analog front end (AFE) amplifier in the past year. The amplifier provides signal conditioning and filtering of the weak neural signals.

Design. Figure 4 shows a block diagram of the complete 16-channel amplifier chip. The differential difference amplifiers (DDA) are used as first stage of the AFE amplifier for high-common-mode rejection ratio (CMRR) and low-noise requirements. A 16:1 multiplexer (MUX) controlled by the clock signal allows all 16 DDAs share the same second and third amplifier/filter stages. The MUX frequency is set to 200 kHz to scan the 16-channel inputs. The second stage and third stage use operational transconductance amplifier (OTA) to implement a low-pass filter, high-pass filter, and gain amplifier with selectable bandwidth and gain. The gain and low-pass filter frequencies are controlled by digital signals: LPF_Select [0:2] and Gain_Select [0:2].
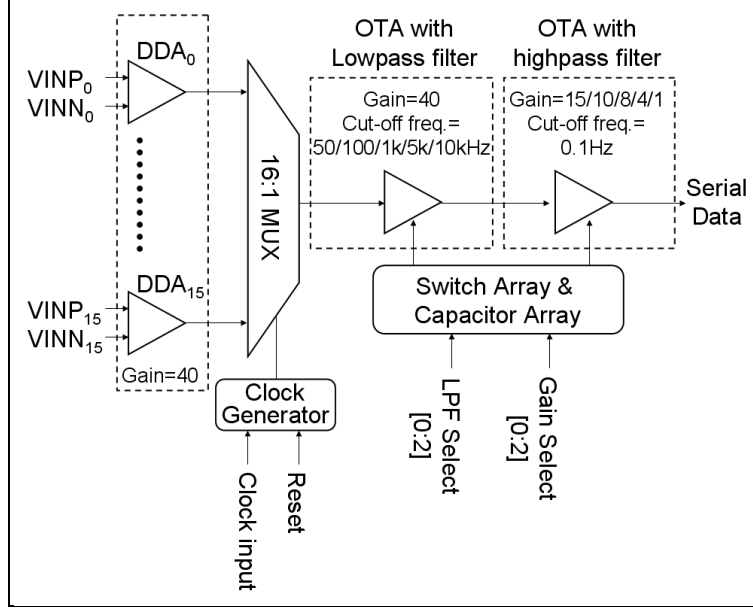
Figure 4. A block diagram of a 16-channel amplifier chip.

The DDA in this amplifier is modified from Ng and Chen (2005), and the circuit is depicted in figure 5. To reduce the original flicker noise, the input stage (M1-M2 and M3-M4) are positive metal-oxide semiconductor (PMOS) with wide width and operated in a weak inversion region. The input stage transfers the input voltage into current. M9 and M10 construct a common source amplifier. The differential currents flowing through M7 and M8 are transferred back to voltage signal by the load device M11 and M12. The output gain stage of DDA is constructed by the two-stage amplifier (M13–M19), which acts as a differential-to-single-ended converter and buffer. C1 and C2 are Miller capacitances used to increase the phase margin. Finally, the DDA-based noninverting amplifier is implemented from the topological placement of R1 and R2. The input/output relation is defined as

$$V_{out} = (R_2/R_1 + 1)V_{in} \qquad (1)$$
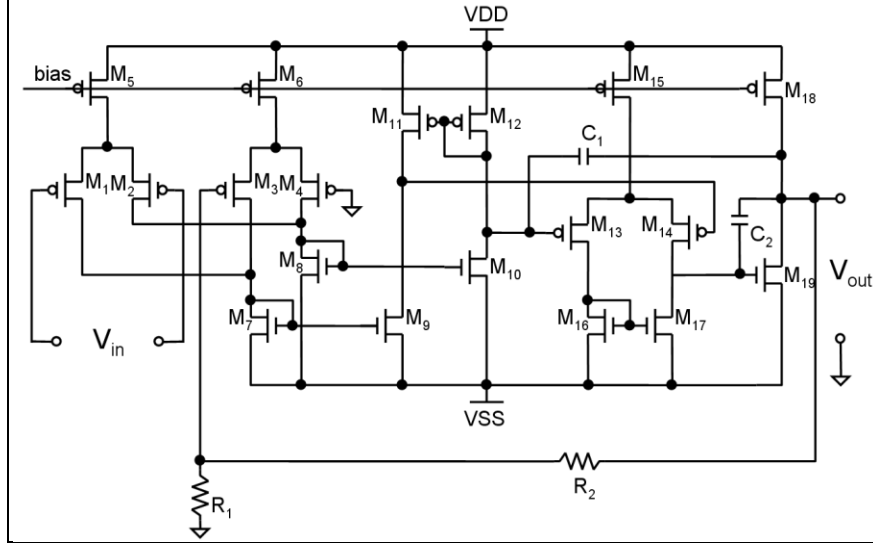
Figure 5. Circuit schematic of the DDA used in present neural amplifier.

Figure 6 shows a schematic of a fully differential OTA used in the second stage and third stage of our 16-channel neural amplifier. The transconductance G_m of the amplifier is controlled by the bias current from M9. The input transistors (M1–M2) are operated in the weak inversion, and the current mirror transistors (M5–M8) are operated in the strong inversion. This design minimizes input-referred noise for a given bias current (Harrison and Charles, 2003). Figure 7 shows the schematic of the second stage, which serves as a programmable low-pass filter. The filter is implemented by two series PMOS transistors across C2 operated in subthreshold region. The mid-band gain AM is set by C1/C2=40. The cutoff frequency is approximately defined as $G_m/(AMCL)$, where G_m is the transconductance of OTA. The selectable on-chip capacitive loads provide 50 Hz to 10 kHz lowpass cut-off frequency.
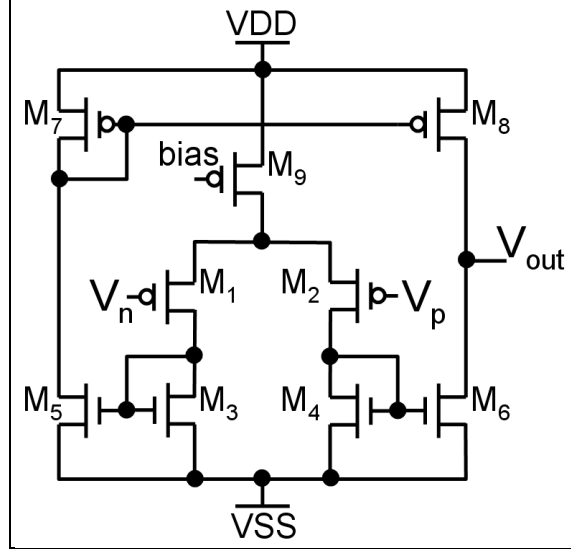
Figure 6. Schematic plot of OTA used in the second
and the third stages.
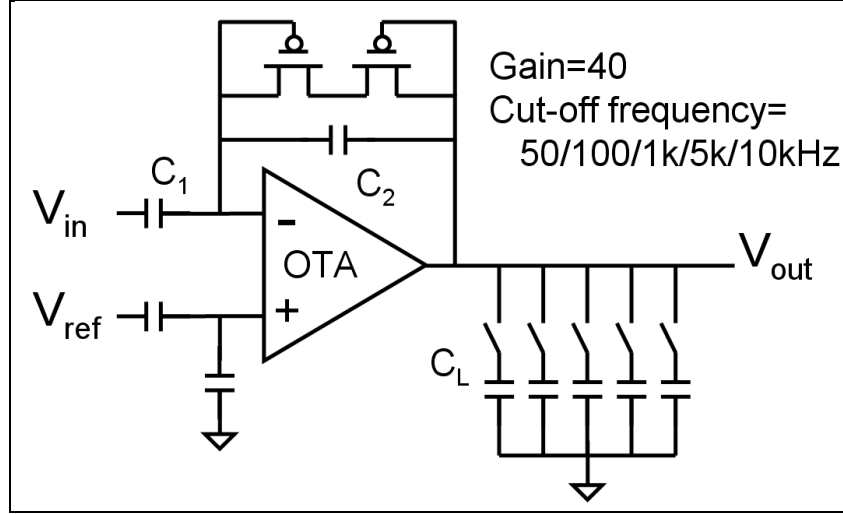
Figure 7. The schematic of the second stage with selectable cutoff frequency.

Figure 8 shows the third amplifier stage with tunable gain and fixed high cutoff frequency. The ratio of capacitors determines the gain factor. The two series PMOS resister across a capacitance is employed to provide the highpass cut-off frequency of 0.1 Hz. The final output of the AFE chip is serial data, of which the packaging volume and wire bonding pads can be reduced due to fewer input/output (I/O) numbers.
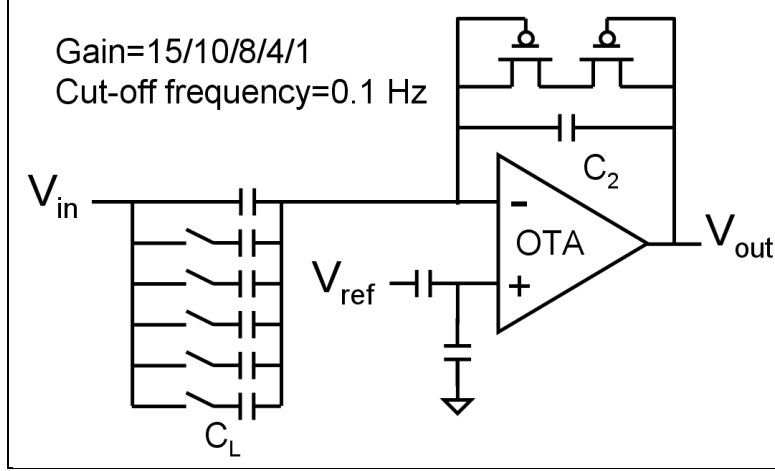
Figure 8. The schematic of the third amplifier stage with tunable gain.

Implementation and fabrication. The 16-channel neural amplifier is fabricated using the TSMC 0.35-μm two-poly four-metal complementary metal-oxide semiconductor (CMOS) process and mounted on a dedicated printed-circuit board for testing. To measure the chip performance, a DAQ device (National Instruments, USA) is used to collect and transmit the 16-channel signal to a laptop. The DAQ device also provides a 200-kHz clock to operate the MUX. A microphotograph of the complete chip is shown in figure 9. The whole chip achieves a size of 4.18 mm^2 including pads. It drains a power of 108 μW when operating for full 16-channel neural recording. The chip operates from a single 1.5-V supply without off-chip components. The measured input referred noise is 2 μVrms in the band of DC to 200 Hz.
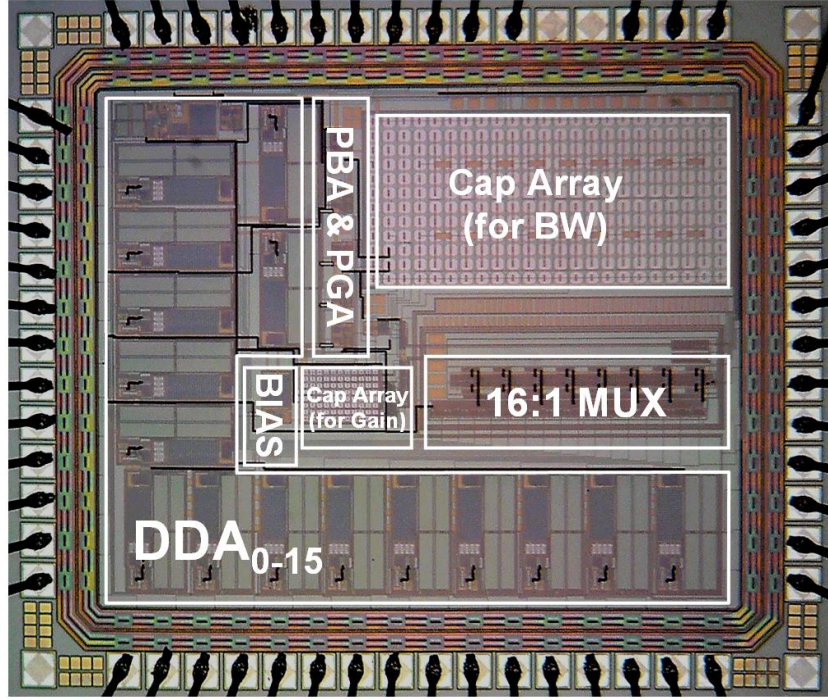
Figure 9. A microphotograph of the complete 16-channel neural amplifier chip.

Testing. We have conducted a comparison study between the physiological signals (simulated electrocardiogram [ECG]) obtained by our custom designed and fabricated low-noise AFE (DDA) and a commercially available 1-channel DDA (LT1789) from Linear Technology (figure 10). The correlation between the two amplified signals was close to 1.
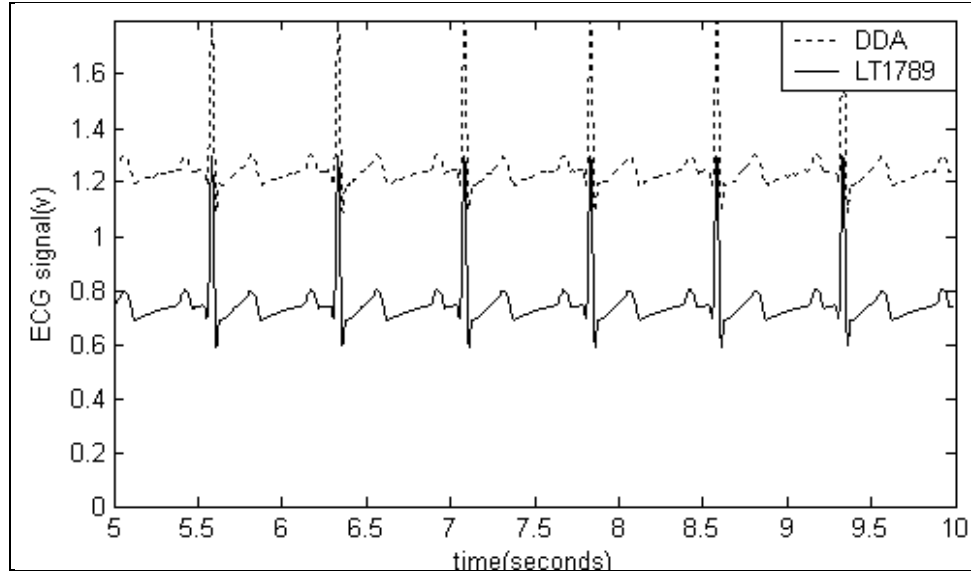
Figure 10. The amplified simulated ECG from our DAA and LT1789 (Linear Technology, Inc).

10

Furthermore, to verify the neural recording capability of the present AFE chip, simultaneous recording performance comparison with commercial integrated circuits (ICs) is tested by using a neural signal simulator (Cyberkinetics, US). A similar three-stage amplifier structure, which consisted of an instrumentation amplifier LT1789 (Linear Technology, U.S.) and two operational amplifiers AD8607 (ADI, U.S.), was used for comparison. Both present AFE chip and commercial ICs provides a band of 0.2–6 kHz with 66 dB in gain. A 100-ms segment of comparison result is shown in figure 11. In figure 11, the upper solid line and the lower dotted line display the results from present neural amplifier and commercial ICs, respectively. These two recordings are highly correlated on average ($r > 0.99$), demonstrating the usefulness of the present chip for neural recording.
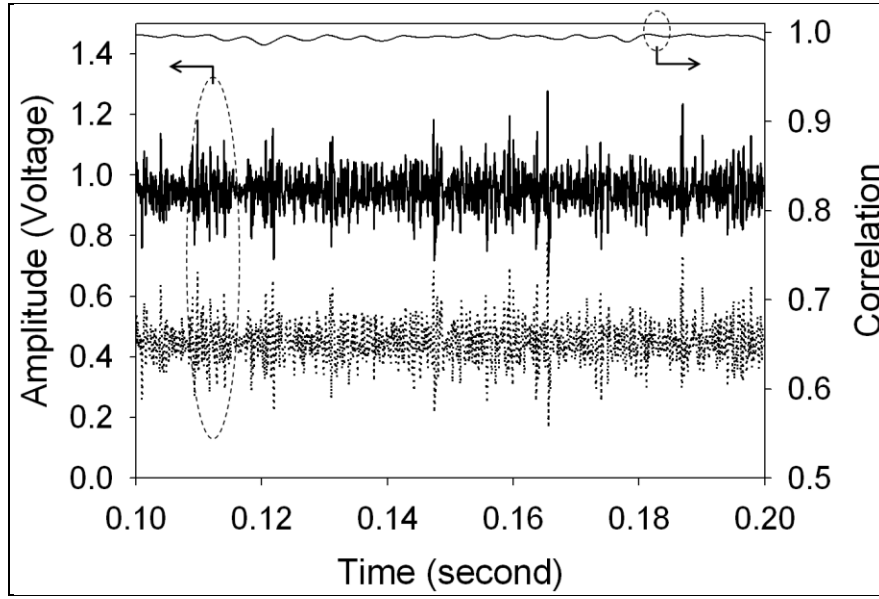
Figure 11. A comparison between our neural amplifier and a commercial IC using signals generated from a neural signal simulator. The solid line and dotted lines show the recordings from our AFE amplifier and the commercial IC, respectively.

Table 1 summarizes the comparison of the measured parameters of this AFE chip with those of reported works. It can be seen that present neural amplifier offers technical merits of reduced supply voltage, sufficient low power per channel, and reasonable low-noise performance, yet offers comparable measured results such as input offset, CMRR and power supply rejection ratio (PSRR).

Table 1. A comparison between our neural amplifier and a commercial IC using signals generated from a neural signal simulator. The solid line and dotted lines show the recordings from our AFE amplifier and the commercial IC, respectively.

	This work		Harrison & Charles, 2003	Harrison, 2007	Aziz et al., 2009	Mollazadeh et al., 2009
Technology	TSMC 0.35 µm		AMI 1.5 µm	AMI 0.6 µm	CMC 0.35 µm	AMI 0.5 µm
	Simulation	Measurement	Measurement	Measurement	Measurement	Measurement
Supply voltage (V)	1.5	1.5	±2.5	5	3	3.3
Current per channel (µA)	4	4.5	16	35	5	12
Power dissipation per channel (µW)	6.1	6.75	13.33	175	15	39.56
Number of channels	16	16	6	16	256	16
Chip area (mm^2)	4.18		0.16	13.33	15.75	9
Mid-band gain (dB)	52–75	48–65	39.5	46	48–68	39.6
High-pass frequency (Hz)	0.1	<0.2	0.025	0.05	0.01–70	0.2–94
Low-pass frequency (Hz)	50–10k	50–6k	7.2k	10–10k	500–5k	140–8.2
Input offset voltage (V)	100n	87.5u	—	±0.6m	—	—
Input common mode range(V)	0.2–1.3	0.26–1.28	—	—	—	—
Input-referred (µVrms)	0.944	2	2.2	2	7	1.94
PSRR (dB)	120	>78	>85	75	-	70
CMRR (dB)	158	>90	>83	84	-	76

1.5   Conclusions

In the past year, our research team has successfully designed and developed dry EEG and fNIR sensors that allow non-invasive and non-intrusive acquisition of EEG and fNIR signals. After numerous simulations and tests, we have finalized the design of the form factor of electro-optode that integrates the EEG and fNIR sensors. We have also fabricated some samples for testing.

1.6   Planned Activities During the Next Report Period

In the next period, we plan to accomplish the following:

1. Conduct a series of in-vitro experiments on pigskin to test the quality of NIR signals acquired by the newly fabricated electro-optodes.

2. Conduct pilot experiments on human fingers/arms and scalp to test the stability of signals acquired by the electro-optodes, the 16-channel AFE very large-scale integration (VLSI) chip and the supporting PCB under different experimental conditions. The goal of this study is to evaluate the penetration rate and efficiency of the NIR lights of the electro-optodes.

2. Project 2: EEG Pattern Classification Using QStates

2.1 Authors

The authors of this project are Anthony J. Ries and Kaleb McDowell of ARL.

2.2 Introduction/Objective

Using patterns of brain activity as indicators of a particular cognitive state offers the potential to monitor and enhance Soldier performance. For example, monitoring brain signals related to Soldier fatigue would assist in determining if the Soldier is alert enough to perform certain cognitively demanding tasks such as operating unmanned aerial vehicles (UAVs). EEG pattern classification has been used to discriminate between a number of cognitive processes. However, before this technology is implemented on the battlefield and decisions are made based on brain state classification, it must be rigorously tested and validated. We recently acquired QStates, a software suite transitioned from the U.S. Army Research Office (ARO), which processes and classifies patterns of EEG. This report summarizes our initial findings on QStates utility in classifying electrical brain activity recorded from two simulated missions.

Figure 12 shows the general process of extracting and applying information from patterns of brain activity collected with EEG to train classification models and classify new data using those models. The raw EEG signal can be processed in real time or offline. The preprocessing step removes signal artifacts such as eyeblinks and high frequency muscle activity, re-references the data, extracts specific signal features such as power spectral density (PSD), and segments the data into epochs. Feature extraction most often entails a linear transformation of the preprocessed epochs to discover patterns that best differentiate the states of interest (e.g., state X versus state Y), while feature selection reduces the feature dimensionality while still trying to obtain high classification performance. The feature extraction and selection process produces a feature vector for each state that is used to train a classifier or is used as input to classify new data. The classification output indicates which state the data likely represent at given timepoints according to the trained model.
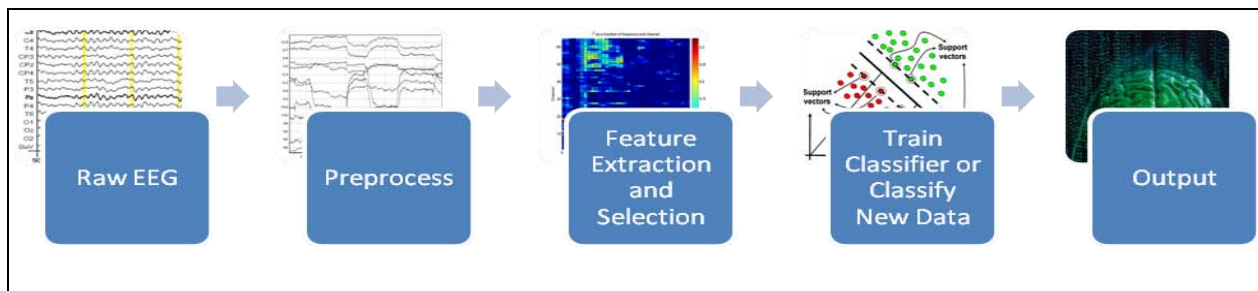

Figure 12. Flow chart depicting the basic process of acquiring, processing, and classifying EEG data.

QStates is a software package for the offline analysis of EEG and other physiological data. It has been designed to process EEG data collected during user-specified cognitive tasks, extract psychophysiological features from the data relevant to a subject's state, and classify patterns of brain activity using either a user-designed classification model or one of three pre-installed normative models developed by the manufacturer. The pre-installed models claim to assess the following cognitive states: Engagement, Workload, and Fatigue. Cognitive Engagement, Workload, and Fatigue are characterized by the following:

- **Engagement**: increase in θ power, decrease in α power

- **Workload**: increase in θ power, decrease in α power (though the magnitudes of the changes are typically to those observed for Engagement)

- **Fatigue**: increase in θ power, decrease in β power

The partial least squares (PLS) algorithm uses features extracted from the physiological data and the ground truths in table 2 as inputs to create the three normative models. A ground truth of zero corresponds to the "Low state" for the classifier, whereas a ground truth of 1 corresponds to the "High state." The Relaxed state is not used when training a classifier for Workload and was therefore assigned an X for its ground truth.

Table 2. Tasks and ground truth assumptions used to create the normative models delivered with the QStates classification software.

Task	Engagement	Workload
Relaxed, Eyes Open	0	X
Column Add (1 digit)	1	0
Column Add (3 digit)	1	1
BattleField2 (no emenies)	1	0
BattleField2 (5 or 6 emenies)	1	1

Many classification software packages contain preinstalled cognitive state models designed from a normative dataset; however, it is not clear how well these models perform when classifying cognitive states from subjects and tasks different from the ones from which they were created. For example, the Qstates software contains a normative workload model that is presumably sensitive to cognitive states associated with low and high workload. This model was created using data from a first-person shooter game and a math task where the low workload classifier was trained on cognitive processes generated from a zero-enemy shooting condition and one-digit addition math task, while the high workload classifier was trained cognitive processes generated from a six-enemy shooting condition and three-digit addition math task. Alternatively, the software allows the user to construct their own models using EEG data from any task to classify on any number of states. This also makes it possible to classify data from the same subjects but from different from those used to develop the classification model. Using models that generalize to other tasks different from those they were trained on assumes, of course, that

the states in the training and testing data are similar. In the present study we compared the classification accuracy of QStates generalized workload model with two user-created models using data obtained from a driving simulation (Experiment 1) as well as an interactive first-person shooter exercise (Experiment 2).

2.3 Experiment 1

2.3.1 Approach: Experiment 1

For Experiment 1, we compared the QStates normative workload model with task-specific individual and group models. Informed consent was obtained prior to experimentation as required by U.S. Army human use regulations (U.S. Department of Defense, 1999; U.S. Department of the Army, 1990). Soldiers performed a visual scanning task under two indirect driving conditions on a ride motion simulator (RMS) while EEG was recorded from a 64-channel BioSemi Active Two system. Soldiers performed two scanning tasks in each condition. In the first condition, coupled motion, there was a direct match between the virtual and physical environments. For example, a Soldier would feel the acceleration of the vehicle on the RMS the instant the Soldier saw it move forward in the simulation. In the other condition, uncoupled motion, what the Soldier felt on the RMS was delayed 11 s from what the Soldier saw in the simulation. It was believed that the uncoupled motion condition would generate distinct brain activation patterns from the coupled motion condition due to the mismatch between physical feedback and visual input.

The Individual model used one of the two tasks within each condition to train the model and performed classification on the other. This was done separately for each individual; therefore, each participant had his/her own model. The task order was counterbalanced for training and classification purposes. The Group model used all subjects' data simultaneously to train model. The Normalized Workload model came preinstalled with the QStates software and used a different sample of subjects who performed the tasks outlined above in table 2. We refer to the coupled motion condition (Individual and Group models) and one-enemy/one-digit addition (Normative Workload model) as "Low" processing state and the uncoupled motion condition (Individual and Group models) and six-enemy/three-digit addition (Normative Workload model) as "High" processing state.

The QStates software outputs a score indicating the probability a given two-second data epoch belongs to the state trained as "High" in the model. In other words if the probability of a given data epoch is above 0.5, then it is more similar to the data used to train the "High" state portion of the model. If the output is below 0.5, the data epoch is more similar to the data used to train the "Low" state portion of the model. Scores nearest to 0.5 indicate the data epoch is unable to be accurately classified according to the model.

2.3.3 Results: Experiment 1

To assess the ability of the models to discriminate between two condition-dependent states (coupled motion/low; uncoupled motion/high), we compared the average probability output for each condition using each model (figure 13). Outputs for coupled and uncoupled motion conditions in the Individual and Norm Workload models were not statistically different from chance classification (all $p > 0.1$). Both conditions in the Group model were significantly different from chance classification, ([Coupled t(9) = −4.4, p = 0.002]; [Uncoupled t(9) = −2.4, p = 0.04]). However, coupled and uncoupled motion output was not significantly different from each other, (t(9) = −1.9, p = 0.08) and the uncoupled motion condition, while different from chance, was classified as more likely to come from the same state produced in the coupled motion condition (i.e., Low).
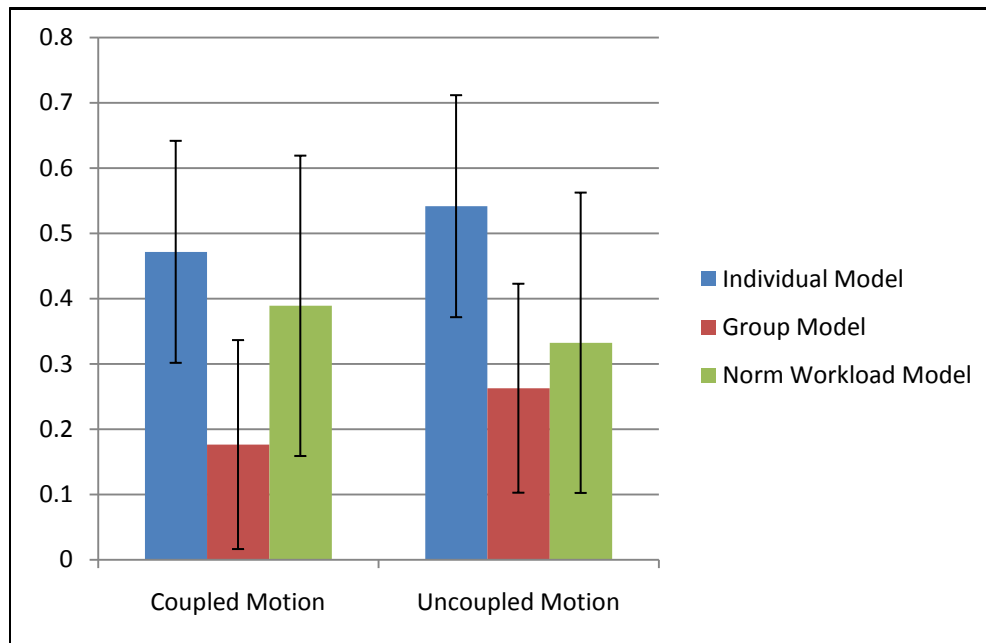
Figure 13. Classification results for the coupled and uncoupled motion conditions using the Qstates Normative Workload model and Individual and Group models. Error bars represent 95% confidence intervals.

2.3.3 Conclusion: Experiment 1

The analysis of the classification data in Experiment 1 suggests the main manipulation in the experiment was not effective, for there were no significant classification differences between the two conditions for any model. This corroborates the behavioral findings that showed no statistically significant difference in reaction time and accuracy between the two conditions. Given the results from Experiment 1 analysis, we analyzed a different dataset that did show an effective experimental manipulation as revealed by significantly different reaction time and accuracy scores in the conditions of interest. Given there were differences in performance, we expected to find these differences reflected in the neural data.

16

2.4 Experiment 2

2.4.1 Approach: Experiment 2

In Experiment 2, we compared the pre-installed Normative Workload model with Individual and Group models generated from 14 marksmen (13 Marines, 1 Soldier). Marksmen performed four separate tasks while EEG was recorded from a 40-channel neuroscan system. The first task, eyes open (EO), required each individual to simply relax with their eyes open. For the second task, subjects performed two-digit math problems, the math (M) condition. In Task 3, shooting (S), each subject performed a first-person shooting task in the Dismounted Infantryman Survivability and Lethality Testbed (DISALT) shooting simulator. In this task the marksmen fired at targets from 50–300 m. In the last task, shooting and math (S&M), the shooters performed both the shooting and math tasks together.

The Individual model used only the individual subject's M and EO data to train model. The Group model used all 14 subjects' M and EO data to train model. The Normalized Workload came preinstalled with the QStates software and used a different sample of subjects who performed the tasks outlined previously. We refer to the EO class (Individual and Group models) and one-enemy/one-digit addition (Normative Workload model) as "Low" processing state and M task class (Individual and Group models) and six-enemy/three-digit addition (Normative Workload model) as "High" processing state.

2.4.2 Results: Experiment 2

The first analysis tested to see if there was a difference between the S and S&M classification output for each model. Based on subjective feedback it was suggested that the S&M task required more mental effort than the S task alone; therefore, we believed the S&M task classification output would be more probable than the S task alone to be classified in the high processing state. Figures 14 and 15 show the output for the S and S&M tasks, respectively, for each model across epochs and Figure 16 shows the means and 95% confidence intervals. Overall, there was no significant difference between S and S&M classification output for the Individual ($t = 0.328$, $p = 0.748$), Group ($t = –0.007$, $p = 0.994$), and Normative Workload ($t = 1.866$, $p = 0.085$). While the Normative Workload model approached significance, the output suggested the S task was more difficult than the S&M task, which is counter to the subjective task difficulty reported by the participants.

The second analysis tested the classification accuracy for each model by comparing the task output to a probability of 0.5. This analysis revealed that only the Individual and Group models produced classification significantly above chance level for both tasks (all $p < 0.01$). The output for the S and S&M tasks was not different from chance classification using the Normative Workload model ($p > 0.1$).

It is important to note that while the training tasks in all models were similar, the Normative Workload model training tasks may have been more difficult or produced greater mental effort in the subject sample. If the S or S&M task required the most mental effort in the testing/classification data but required less mental effort when compared to the high mental effort task in the Normative Workload model, then it is not surprising that the S and S&M output had a lower probability of being in the high state when using the Normative Workload model. In other words, the classification output is dependent upon the training data used in the model. If the training data between two models are different and reflect different degrees of cognitive processing initially, then it would not be surprising to get different classification output as well. This is a key concern when employing normative models especially when the specifics of the training data are unknown.
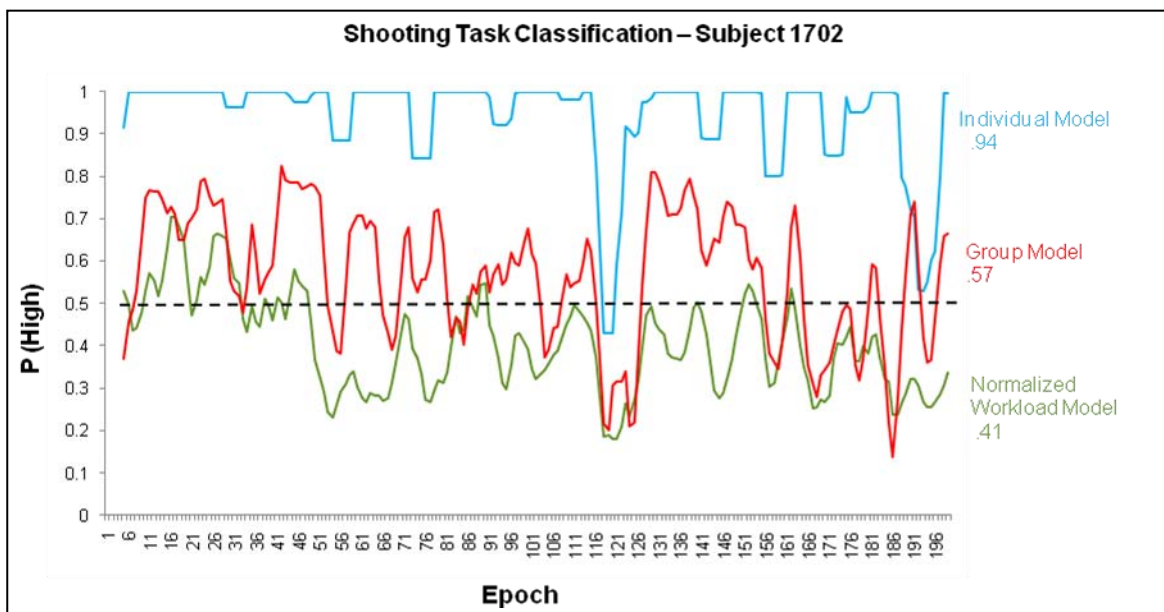
Figure 14. Classifier output over the course of the S task for a single subject.
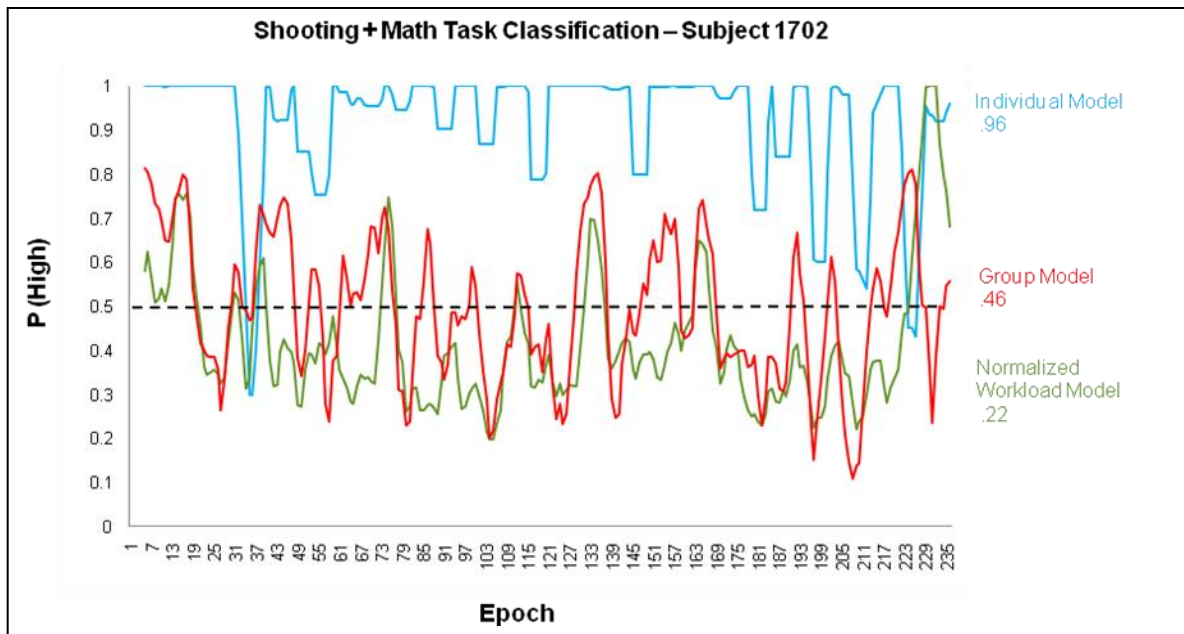
Figure 15. Classifier output over the course of the S&M task for a single subject.
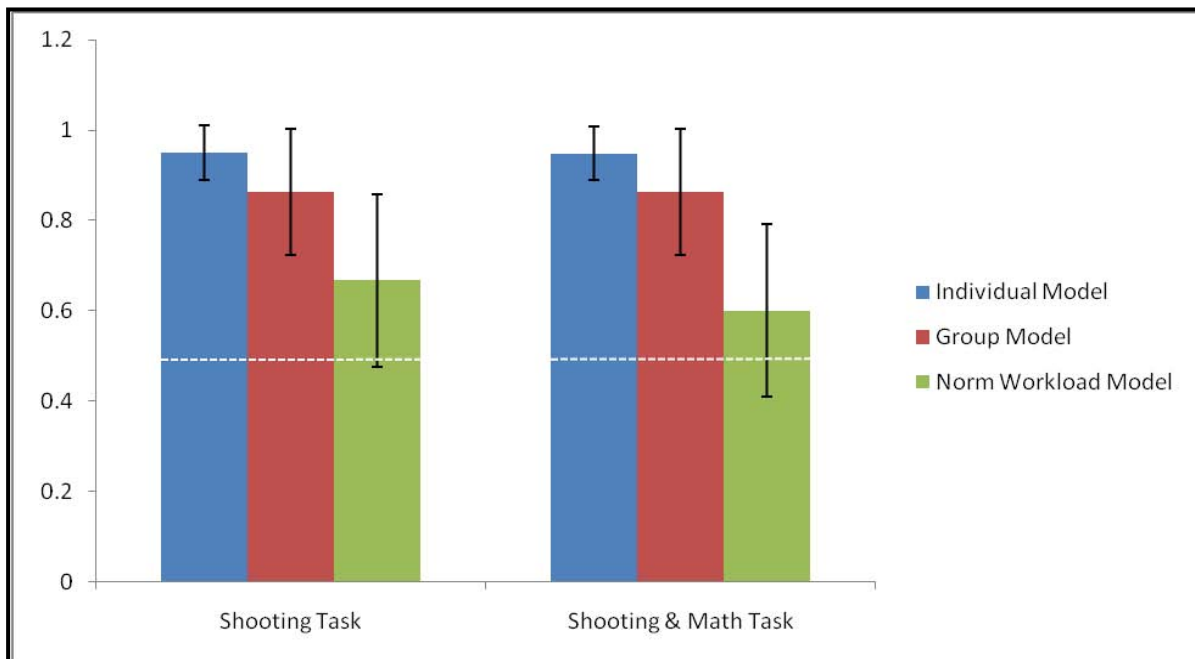
Figure 16. Classification results for the S and S&M tasks using the Qstates Normative Workload model and individual and group models trained on the EO and M tasks. Error bars represent 95% confidence intervals.

Workload related brain activity is sensitive to changes in mental effort devoted to a particular task. In the current tasks, it is likely that the S&M task required more mental effort than the S task alone; however, the classification output from the Normative Workload model suggests the

19

opposite is true. This brings into question the external validity of the Normative Workload model and reinforces the idea that normative models of workload are not always consistent with the ground truth.

4.2.3 Conclusions: Experiment 2

Due to the high variability in brain activity between individuals, it is recommended that Individual models are used. Group and Normative models generally produce lower classification accuracy compared to Individual models, and therefore, output based on Group and Normative models should be interpreted with caution. Moreover, it is essential that the researcher know what tasks were used in creating normative pre-installed models, for not all tasks require cognitive processes that are easily generalizable.

Our suggestions for more enhanced classification software are as follows:

- Enable the user to perform event-related classification.
- Offer more algorithm selections such as Support Vector Machines (SVM).
- Increase number of subjects and tasks used to create the normative QStates models.
- Incorporate temporal aspects of cognitive processes into possible classification parameters.

3. Project 3: Non-linear Brain Activity in Real-world Settings: Movement Artifact and the Phase Lag Index

3.1 Authors

The authors of this project are Kaleb McDowell, Scott E. Kerick, and Kelvin Oie.

3.2 Introduction/Objective

The brain is a complicated network comprised of neural systems that function to meet two diverse requirements: the local specialization of assemblies of neurons for specific types of information processing and the integration of information at a more global level (Friston, 1994; Sporns, Tononi, and Edelman, 2000). Recently, it has been argued that, in order to advance our current understanding of functional brain dynamics, a more large-scale, integrative systems view is required (Le van Quyen, 2003; Varela, Lachaux, Rodriguea, and Martinerie, 2001). Recently, novel approaches have started to be implemented to examine the nervous system at this integrative level. For example, the rise of network science (Albert and Barabasi, 2002; Borner, Sanyal, and Vespignani, 2007; Newman, 2003; Strogatz, 2001; Watts and Strogatz, 1998) has contributed novel approaches that are now being applied to examine brain function at an integrated global level (de Haan et al., 2009; De Vico Fallani et al., 2007; Reijneveld, Ponten, Berendse, and Stam, 2007; Stam, 2007, 2010).

One of the critical components of any approach underlying an integrative systems view will be to understand the connectivity between local regions within the nervous system. Traditional techniques to examine this connectivity, such as cross-correlation and coherence, are based on linear techniques. However, it has been posited that coordinated neural activity may be related through nonlinear functions, including those with strong transients or cross-frequency phase locking (Friston, 2000; Palva, Palva, and Kaila, 2005; Stam, Breakspear, van Cappellen van Walsum, and van Dijk, 2003), and traditional linear techniques are limited by their inability to detect nonlinear interdependencies between the underlying dynamical systems, their unsuitability to characterize non-stationary data with rapidly changing interdependencies, and the potential bias for high correlations among EEG recording electrodes due to volume conductive properties of the cerebral-spinal fluid, meninges, skull, and scalp (Stam et al., 2009; Stam and van Dijk, 2002). One new nonlinear measure of functional connectivity that purportedly circumvents these issues is the phase lag index (PLI) (Stam, Nolte, and Daffertshofer, 2007). PLI is a measure of the asymmetry of the distribution of phase differences between two signals and is less affected by volume conduction than traditional linear measures such as coherence and nonlinear measures such as synchronization likelihood. This is because PLI assumes that the phase lag of volume-conducted signals is near-instantaneous (i.e., zero phase) (Stam et al., 2007; Stam et al., 2009) and, therefore, non-zero phase relationships observed between two interdependent signals cannot be attributed to volume conduction, but may be attributed to a functional relationship between them.

Thus, although promising, PLI has only been applied to small segments of artifact-free EEG data, which potentially limits its application, especially with regards to understanding brain networks of Soldiers performing tasks in operational environments where artifacts are unavoidable. Accordingly, the purpose of this study was to apply PLI analyses to EEG data recorded from participants under conditions of varying levels of motion characteristic of operational environments. Specifically, we subjected participants to stationary (sitting still) and dynamic vehicle motion simulation conditions (sitting in a seat while traversing over a paved "washboard" road surface and traversing over irregular "cross-country" terrain) and stationary (standing still) and dynamic ambulatory conditions (walking and jogging on a treadmill).

3.3 Approach

3.3.1 Subjects

The test participants were normal adult right-hand, right-eye-dominant males (N = 5; age range 27–39). The voluntary, fully informed consent of the persons used in this research was obtained as required by U.S. Army human use regulations (U.S. Department of Defense, 1999; U.S. Department of the Army, 1990).

3.3.2 Motion Environments

A RMS was used to simulate vehicle motion environments. The RMS uses a MOOG 6 degree-of-freedom (6-DOF) 20000E motion platform (MOOG, East Aurora, NY), capable of producing dynamics similar to that of military ground vehicles traversing over secondary roads and cross-country terrain. It is comprised of a platform mounted on a hexapod actuator design that is securely fixed to a non-movable surface and produces motions in the longitudinal, lateral, vertical, roll, pitch, and yaw directions with maximal acceleration limited to ±0.6 g lateral and longitudinal and −0.5 to 0.7 g vertical. A treadmill (Quinton, Bothell, WA) was used to simulate ambulatory motion environments.

3.3.3 Electroencephalography

Continuous EEG data were acquired using a 24-bit, 40-channel ActiveTwo amplifier with ActiView software and an electrode cap (Active Headcap) with pre-amplified surface electrodes. A water-soluble electrode gel (Signa Gel; Parker Laboratories, Inc., Fairfield, NJ) was inserted into each of the electrode casings to facilitate conductivity between the scalp and electrode surfaces. EEG data were recorded from 32 electrode sites referenced to a common mode sense (CMS) electrode with the midline frontopolar electrode (FPz) as ground. Data were re-referenced offline to averaged mastoids (A1, A2). Electrode impedances were maintained under 10 kΩ. The sampling rate for analog-to-digital conversion was 512 Hz and band pass filtered at 0.016–100 Hz online. Vertical (VEOG) and horizontal (HEOG) electro-ocular activity was recorded using bipolar montages attached superior and inferior to the right eye and both orbital fossa.

3.3.4 Task and Conditions

The experiment consisted of an auditory discrimination task using the "oddball" paradigm (Polich and Kok, 1995; Polich, 1997), which the participants performed in each of six motion environment conditions. In each motion environment condition, a total of 100 auditory stimuli (target and non-target stimuli) were presented once every 3.5–6.5 s in a random series with the target stimuli (2000 Hz) occurring less frequently (probability = 0.20) than the non-target (1000 Hz; probability = 0.80) stimuli. All auditory stimuli were 50 ms in duration and presented at 60 dB. Inter-stimulus intervals were varied to reduce the likelihood of habituation via expectancy effects (Yordanova and Kolev, 1997). The auditory stimuli were generated by a personal computer running E-Prime (ver. 1.1; Psychology Software Tools, Inc., Pittsburgh, PA) and presented binaurally to the participants via stereo headphones, which were worn throughout all task conditions. The participants held a modified bicycle grip (analogous to a gaming joystick) in their right hand and were instructed to press a button, which was attached to the top of the grip, with their thumb as quickly as possible in response to target stimuli and to not respond to non-target stimuli. Participants were instructed to fixate on a spot marked directly in front of them at eye-level. Response times were recorded as the time interval between the onset of target stimuli and the time of each relevant button press. Response errors (i.e., the

combination of percent failures to respond to target stimuli and the percent of responses to non-target stimuli) were also recorded.

The six motion environment conditions included three vehicle motion environments and three ambulatory motion environments. For the vehicle motion environments, a "control" condition required the participants to perform the auditory discrimination task from a static seated position in a chair mounted on the RMS platform with no motion. In a low vehicle motion condition, the participants performed the task while riding on the RMS simulating a wheeled vehicle traversing over a paved washboard road surface and in a high motion condition simulating a tracked vehicle traversing cross-country terrain. For the ambulatory motion environments, the participants performed the auditory discrimination task while standing still on a treadmill with no motion (0 mph), while walking on a treadmill (3 mph), and while jogging on a treadmill (5 mph) (for more details see Kerick, McDowell, and Oie, 2009). A 2-min warm-up was provided for the jogging condition to minimize risk of injury by gradually increasing the treadmill up to speed. The sequence of conditions was assigned randomly within blocks of RMS (control, paved, and cross-country) and treadmill (standing, walking, and jogging) environments and blocks of RMS and treadmill conditions were counterbalanced to minimize order effects. Each task condition was ~6 min in duration, with 5-min rest provided between each task performance. The total time to complete the experimental session was 90–120 min.

3.4 Results

In a previous effort (Kerick, Oie, and McDowell, 2009), we investigated whether we could derive reliable event-related potentials (ERPs) in each of the environments and found that ERPs could not be reliably obtained in the cross-country vehicle motion and walking and jogging ambulatory conditions using standard methods because of excessive artifacts observed in these conditions. However, that effort revealed no differences in behavioral measures in any of the six conditions.

Here, we attempt to understand the susceptibility of PLI to the motion artifacts generated in these six environments. However, due to the novel nature of the PLI measure, the PLI methods will be intertwined with the results.

To give a general concept of the artifacts in this study, figure 17 is presented which is a sample of 10 s of "nearly" raw data from each of the six conditions. Generally, the raw data from the sitting, paved, and standing conditions are similar; however, artifacts can be observed directly in the other three conditions including the stride frequency being clearly evident in the jogging condition (see Kerick et al., 2009, for details).
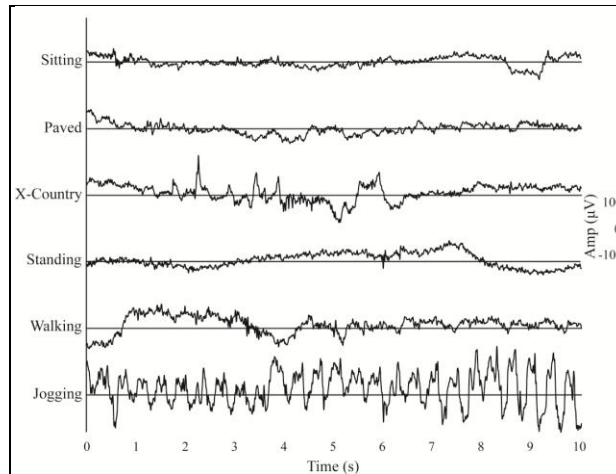
Figure 17. EEG data at Cz from a single participant after
0.01–40 Hz band pass filtering and eye-blink reduction.
Each line represents a continuous 10-s segment of
data from within each environment (figure from
Kerick et al., 2009). Note that eye-blink reduction.

Consistent with Stam et al. (2007), the raw EEG data were first filtered into six standard EEG frequency bands (delta [0.5–4 Hz], theta [4–8 Hz], alpha 1 [8–10 Hz], alpha 2 [10–13 Hz], beta [13–30 Hz], and gamma [30–45 Hz]) using a finite impulse response filter. PLI was then calculated using a Hilbert transform and formulas from Stam et al. (2007). Underlying each estimate of PLI is a phase estimate over a given reference (RF) window length. To examine the effect of RF on PLI, PLIs for a single electrode pair were continually calculated for multiple RFs from 250 ms to 8 s in 250-ms intervals. For each window length, PLIs were estimated multiple times within a 16-s epoch by stepping through the epoch at 250-ms increments resulting in 63 PLI estimates for the smallest RF and 33 estimates for the longest RF.

As can be seen in figure 18, as RF changes, the variability of the PLI estimate can change, further as RF increases, PLI decreases.
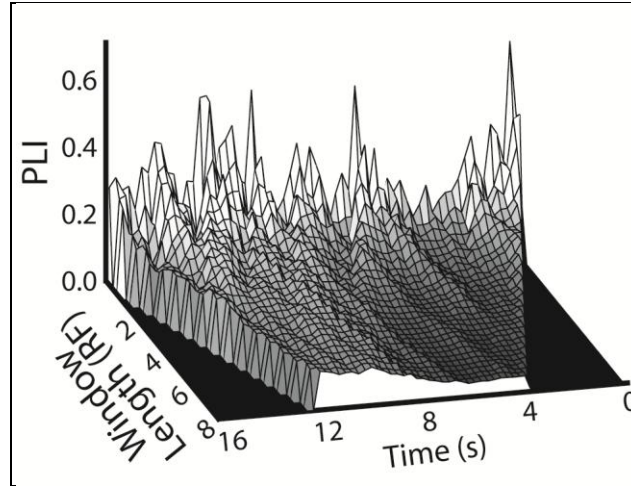
24

Figure 18. PLI estimates at a single electrode pair from a
single participant. High variability and high
amplitude is observed in PLIs calculated with
small (250-ms) RF.

For further analyses, PLI was calculated using an RF of 500 ms in 250-ms intervals for each
electrode pair and for each frequency bin. PLIs were calculated within 16-s epochs centered on
each stimulus presentation resulting in 61 PLI estimates for each stimulus to attempt to
understand the susceptibility of PLI to the motion artifacts generated in the six environments.
Here, mean PLI were calculated across all participants, all electrode pairs, time, and both
stimulus types. Figure 19 illustrates a normalized version of these means for each condition and
for each frequency band. Normalization was achieved by subtracting the mean from the sitting
condition from that for each condition; as such, the normalized PLIs for the sitting condition are
zero. Further, there are several options for representing the variance of these data (e.g., across
participants, electrode pairs, time). Here, we choose to present the standard deviation across the
16-s epochs prior to averaging across participants and electrode pairs to reflect how the measure
generally varies on a moment to moment basis (between participants variance is presented in
figure 20). While it is clear that we cannot definitively differentiate between the susceptibility of
PLI to motion artifact versus differences in neural process in these conditions, we believe that
this illustration effectively describes the generic behavior of the measure across the six
environments examined here.
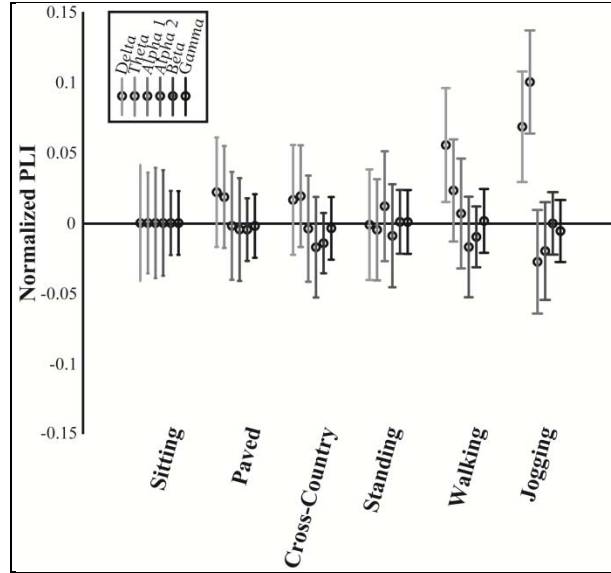
Figure 19. Normalized PLI estimates for all participants,
all electrode pairs, and both stimulus types.
Within each condition, frequencies from left to
right are ordered from delta to gamma band
(low to high). Bars reflect the mean standard
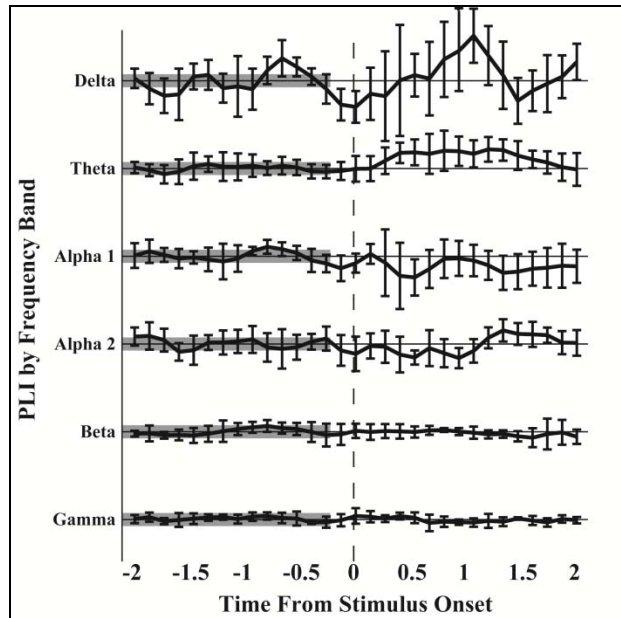deviations across epochs.

Figure 20. Event-related PLI estimates for all participants,
all electrode pairs, and the target stimuli.
Stimulus onset occur here at time = 0, however,
due to the RF = 500 ms, some effect of the stimulus
maybe seen as early as −250 ms (gray bar reflects
true pre-stimulus period).

26

Figure 19 illustrates that PLI in the two lowest frequency bands were affected by motion in the ambulatory condition and minimally impacted in the vehicle motion conditions (see mean plus standard deviation above zero). PLI in the higher four frequency bands appeared to be minimally, if at all, impacted by any of the motion conditions. Importantly, it should be noted here that while stride frequency and the movement itself in these conditions are generally associated with low frequencies ($\leq$delta activity), muscle activity associated with physical motion, generally, is associated with higher frequency activity ($\geq$ alpha activity).

The previous data suggest that on a global level, across the entire set of conditions examined here, PLI appears only slightly sensitive to lower frequencies and appears insensitive to the higher frequencies. The question thus remains, however, is PLI sensitive to anything in the tasks themselves (previous literature has suggested that PLI is sensitive to particular disease states—Stam et al. 2009; Stam et al 2007)? To address this question, a novel event-related analysis of PLI is illustrated in figure 20. In this figure, time-evolving PLI is depicting starting approximately 2 s prior to target stimuli onset. Mean values at each time step are depicted with error bars reflecting the between participants standard deviation. A pre-stimulus baseline is represented from –2.0 to –0.25 s. In the lowest four frequencies, it can be observed that generally there is more variance in the waveforms after the onset of the stimulus. Further, in several cases, the mean plus standard deviation does not cross the baseline boundary. These results suggest that PLI, even at this gross level, is capable of reflecting sensitivity to stimulus processing.

3.5   Conclusions

The primary goal of this project is to enable approaches to advance our current understanding of functional brain dynamics in operationally relevant settings by investigating a metric that (1) can underlie a large-scale, integrative systems approach, (2) has sensitvity to neurocognitive processing, and (3) has low sensitivity to signal artifacts generated from biological and environmental sources while recording EEG data in real-world environments. PLI is a nonlinear measure of functional connectivity that has been demonstrated to provide the basis for such a large-scale, integrative approach (Stam et al., 2009). Futher, as PLI examines only non-zero phase relationships, it is purportedly not sensitive to volume conduction (Stam et al., 2007). The data presented here are generally supportive of this claim and provide preliminary evidence that PLI is also sensitive to basic neurocognitive processing.

We illustrate that on a global level, low-frequency PLI has slight sensitivity to self-generated motion (i.e., walking and jogging); however, mid- and high-frequency PLI do not show such sensitivity to any motion condition. The slight sensitivity of PLI in the lower frequencies could reflect either the neurocognitive processing associated with self-generated motion or could reflect artifacts from these conditions. Importantly, as the higher frequency PLIs do not reflect such sensitivity, it seems unlikely that the lower frequency PLIs are directly reflecting muscle activity. Overall, these results suggest that PLI can be used to reliably examine brain electrical data in certain operational environments such as driving. At this time, careful interpretation is

necessary in ambulatory vehicle motion environments. A more specific, network-based analyses of the data presented here may provide insights into the source of the apparent low frequency sensitivity and potentially enable the broader application of the PLI metric.

We further illustrate that aspects of PLI (i.e., either the PLI value or its variability) appear sensitive to short-duration neurocognitive processing. Considering (1) the variability in estimating phase in the 500-ms RF here and (2) the very general nature of this exploratory analysis, this result is very promising and supports the investigation of PLI in a large-scale, integrative systems approach.

The positive results presented here support a novel approach to overcoming artifact issues and present alternative perspectives on understanding brain behavior. Such results here give hope that PLI can be applied within military-relevant environments and augment Soldier state and neurocognition monitoring technologies. The use of a nonlinear metric of functional connectivity also holds the promise of novel real-time insights that can be used to drive and improve current conceptions of brain-machine adaptive training and operational systems and in-field neurocognitive assessment.

4. References

Albert, R.; Barabasi, A. L. Statistical Mechanics of Complex Networks. *Rev. Mod. Phys.* **2002**, *74*, 47–97.

Aziz, J.; et al. 256-Channel Neural Recording and Delta Compression Microsystem with 3D Electrodes. *IEEE Journal of Solid-State Circuits* **2009**, *44* (3).

Borner, K.; Sanyal, S.; Vespignani, A., 2007: Network Science, In Blaise Cronin (Ed) Annual Review of Information Science & Technology, Volume 41. Medford, NJ: Information Today, Inc./American Society for Information Science and Technology, chapter 12, pp. 537–607.

de Haan, W.; Pijnenburg, Y.A.L.; Strijers, R.L.M.; van der Made, Y.; van der Flier, W. M.; Scheltens, P.; Stam, C. J. Functional Neural Network Analysis in Frontotemporal Dementia and Alzheimer's Disease Using EEG and Graph Theory. *BMC Neurosci.* **2009**, *10*, 101.

De Vico Fallani, F.; Astolfi, L.; Cincotti, F.; Mattia, D.; Tocci, A.; Marciani, M. G.; Colosimo, A.; Salinari, S.; Gao, S.; Cichocki, A.; Babiloni, F. Extracting Information from Cortical Connectivity Patterns Estimated from High Resolution EEG Recordings: A Theoretical Graph Approach. *Brain Topog.* **2007**, *19*, 125–136.

Friston, K. J. Functional and Effective Connectivity in Neuroimaging: A Synthesis. *Hum. Brain Mapp.* **1994**, *2*, 56–78.

Friston, K. J. The Labile Brain: Neuronal Transients and Nonlinear Coupling. *Phi. Trans. Royal Soc. London Series B: Biol. Sci.* **2000**, *355*, 215–236.

Harrison, R. R.; Charles, C. A low-power Low-noise CMOS Amplifier for Neural Recording Applications. *IEEE J. Solid-State Circuits* **2003**, *38* (6), 958–965.

Harrison, R. R. A Versatile Integrated Circuit for the Acquisition of Bipotentials. *IEEE Custom Integrated Circuits Conference CICC*, pp. 115–122, 2007.

Huang-Hellinger, F. R.; Breiter, H. C.; McCormack, G.; Cohen, M. S.; Kwong, K. K.; Sutton, J. P.; Savoy, R. L.; Weisskoff, R. M.; Davis, T. L.; Baker, J. R.; Belliveau, J. W.; Rosen, B. R. Simultaneous Functional Magnetic Resonance Imaging and Electrophysiological Recording. *Hum. Brain Mapp.* **1995**, *3*, 13–23.

Ives, J. R.; Warach, S.; Schmitt, F.; Edelmann, R. R.; Schomer, D. L. Monitoring the Patient's EEG During Echo Planar MRI. *Electroenceph. Clin. Neurophysiol.* **1993**, *87*, 417–420.

Kerick, S. E.; Oie, K.; McDowell, K. *Assessment of EEG Signal Quality in Motion Environments*; ARL-TR-4866; U.S. Army Research Laboratory: Aberdeen Proving Ground, MD, 2009.

Le van Quyen, M. Disentangling the Dynamic Core: A Research Program for a Neurodynamics at the Large-Scale. *Biol. Res.* **2003***, 36*, 67–88.

Lemieux, L.; Allen, P. J.; Franconi, F.; Symms, M. R.; Fish, D. R. Recording of EEG During fMRI Experiments: Patient Safety. *Magn. Reson. Med.* **1997**, 38, 943–952.

Mollazadeh, M.; et al. Micropower CMOS Integrated Low-Noise Amplification, Filtering, and Digitization of Multimodal Neuropotentials. *IEEE Transactions on Biomedical Circuit and Systems* **2009**, *3* (1).

Newman, M.E.J. The Structure and Function of Complex Networks. *Soc. Indust. Appl. Math. Rev.* **2003***, 45*, 197–256.

Ng, K. A.; Chan, P. K. A CMOS Analog Front-end IC for Portable EEG/ECG Monitoring Applications. *Analog Integrated Circuits and Signal Processing* **2005**, *42*, 65–76.

Palva, J. M.; Palva, S.; Kaila, K. Phase Synchrony Among Neuronal Oscillations in the Human Cortex. *J. Neurosci.* **2005***, 25*, 3962–3972.

Polich J.; Kok, A. Cognitive Determinants of P300: An Integrative Review. *Biol. Psychol.* **1995***, 41*, 103–146.

Polich, J. On the Relationship Between EEG and P300: Individual Differences, Aging, and Ultradian Rhythms. *Int. J. Psychophysiol.* **1997***, 26*, 299–317

Reijneveld, J. C.; Ponten, S. C.; Berendse, H. W.; Stam, C. J. The Application of Graph Theoretical Analysis to Complex Networks in the Brain. *Clin. Neurophysiol.* **2007***, 118*, 2317–2331.

Sporns, O.; Tononi, G.; Edelman, G.M. Theoretical Neuroanatomy: Relating Anatomical and 6 Functional Connectivity in Graphs and Cortical Connection Matrices. *Cerebral Cortex* **2000***, 10*, 127–141.

Stam, C. J. Use of Magnetoencephalography (MEG) to Study Functional Brain Networks in Neurodegenrative Disorders. *J. Neurol. Sci.* **2010***, 289*, 128–134.

Stam, C. J.; Breakspear, M.; van Cappellen van Walsum, A. M.; van Dijk, B. W. Nonlinear Synchronization in EEG and Whole-head MEG Recordings of Healthy Subjects. *Hum. Brain Mapp.* **2003***, 19*, 63–78.

Stam, C. J.; de Haan, W.; Daffertschofer, A.; Jones, B. F.; Manshanden, I.; van Cappellen van Walsum, A. M.; Montez, T.; Verbunt, J.P.A.; de Munck, J. C.; van Dijk, B. W.; Berendse, H. W.; Scheltens, P. Graph Theoretical Analysis of Magnetoencephalographic Functional Connectivity in Alzheimer's Disease. *Brain* **2009**, *132*, 213–224.

Stam C. J.; Jones, B. F.; Nolte, G.; Breakspear, M.; Scheltens, P. Small-Word Networks and Functional Conectivity in Alzheimer's Disease. *Cerebral Cortex* **2007**, *17*, 92–99.

Stam, C. J.; Nolte, G.; Daffertschofer, A. Phase Lag Index: Assessment of Functional Connectivity from Multi Channel EEG and MEG with Diminished Bias from Common Sources. *Hum. Brain Mapp.* **2007**, *28*, 1178–1193.

Stam, C. J.; Reijneveld, J. C. Graph Theoretical Analysis of Complex Networks in the Brain. *Nonlin. Biomed. Physics* **2007**, *1–3*, doi:10.1186/1753-4631-1-3.

Stam, C. J.; van Dijk, B. W. Synchronization Likelihood: an Unbiased Measure of Generalized Synchronization in Multivariate Data Sets. *Physica D* **2002**, *163*, 236–241.

Strogatz, S. H. Exploring Complex Networks, *Nature* **2001**, *410*, 268–276.

U.S. Department of the Army, 1990: Use of Volunteers as Subjects of Research; AR 70-25; Government Printing Office: Washington, DC.

U.S. Department of Defense, 1999: Code of Federal Regulations: Protection of Human Subjects; 32 CFR 219; Office of the Secretary of Defense, Government Printing Office: Washington, DC.

Varela, F.; Lachaux, J. P.; Rodriguez, E.; Martinerie, J. The Brainweb: Synchronization and Large-Scale Integration. *Nat. Rev. Neurosci.* **2001**, *2*, 229–239.

Watts D. J.; Strogatz, S. H. Collective Dynamics of "Small-world" Networks. *Nature* **1998**, *393*, 440–442.

Yordanova, J.; Kolev, V. Developmental Changes in the Event-related EEG theta Response and P300. *Electroencephal. Clin. Neurophysiol. Evoked Potentials Section* **1997**, *104*, 418–430.

List of Symbols, Abbreviations, and Acronyms

2-D	two-dimensional
3-D	three-dimensional
6-DOF	6 degree-of-freedom
AFE	analog front end
ARO	Army Research Office
BOLD	blood-oxygen-level dependence
CMOS	complementary metal-oxide semiconductor
CMRR	common-mode rejection ratio
CMS	common mode sense
DAQ	data acquisition
DDA	differential difference amplifiers
DISALT	Dismounted Infantryman Survivability and Lethality Testbed
ECG	electrocardiogram
EEG	electroencephalogram
EMG	electromyogram
EO	eyes open
ERPs	event-related potentials
fMRI	functional magnetic resonance imaging
fNIRS	functional near infrared spectroscopic
I/O	input/output
ICA	Independent Components Analysis
ICs	integrated circuits
LED	light-emitting diode
M	Math

MEMS   Micro-electromechanical system

MR   magnetic resonance

MUX   multiplexer

NIR   near infrared

OTA   operational transconductance amplifier

PCB   printed circuit board

PDs   photodiodes

PLI   phase lag index

PLS   partial least squares

PMOS   positive metal-oxide semiconductor

PPG   photoplethysmography

PSD   power spectral density

PSRR   power supply rejection ratio

RF   reference

RMS   ride motion simulator

S   shooting

S&M   shooting and math

SVM   Support Vector Machines

UAV   unmanned aerial vehicle

VLSI   very large-scale integration